ADVANCED THEORY AND SIMULATIONS
www.advtheorysimul.com

Nanoporous Morphogenesis in Amorphous Carbon Layers: Experiments and Modeling on Energetic Ion Induced Self-Organization

*Daniel T. Hoffmann, Johannes Dietrich, Stephan Mändl, Mareike Zink, and Stefan G. Mayr**

Nanoporous amorphous carbon constitutes a highly relevant material for a multitude of applications ranging from energy to environmental and biomedical systems. In the present work, it is demonstrated experimentally how energetic ions can be utilized to tailor porosity of thin sputter deposited amorphous carbon films. The physical mechanisms underlying self-organized nanoporous morphogenesis are unraveled by employing extensive molecular dynamics and phase field models across different length scales. It is demonstrated that pore formation is a defect induced phenomenon, in which vacancies cluster in a spinodal decomposition type of self-organization process, while interstitials are absorbed by the amorphous matrix, leading to additional volume increase and radiation induced viscous flow. The proposed modeling framework is capable to reproduce and predict the experimental observations from first principles and thus opens the venue for computer assisted design of nanoporous frameworks.

1. Introduction

Nanoporous carbon has attracted rapidly growing interest during the past decades as electrode, supercapacitor, sensor, catalyst support, filter/sieve, gas, and liquid adsorption/storage, as well as biomedical material for a broad range of applications, including in the first place energy conversion and environment (see, e.g., refs. [1–6] for overviews and recent promising examples). Traditionally bulk porouos carbon is typically synthesized by physical, chemical and catalytic activation or carbonization.[7] When heading for miniaturized, for example, on chip integration, nanoporous thin films that are synthesized by employing techniques established in semiconductor industry are highly desirable. In the present manuscript we will demonstrate how ion implantation into sputter deposited amorphous carbon (a–C) can be utilized to obtain a nanoporous morphology that is highly tunable by the choice of implantation parameters and temperature. Besides experimental phenomenology, our central focus will be laid on the physical foundations of nanoporous morphogenesis. This is achieved by a combined approach that couples classical molecular dynamics calculations to a novel phase field model, thus bridging different length and time scales.

Generally, ion implantation induced nanoporous morphogenesis constitutes a phenomenon that has previously most prominently been reported for implantation into amorphous germanium (see Ref. [8–13] and references therein); besides that it bears some similarity to void lattice formation observed under high fluence conditions in metals,[14,15] however at much larger doses. Contrarily, nanoporous morphogenesis is not established at this point in a–C, presumably due to the requirement of an elevated temperature, as we will demonstrate in detail in the following.

2. Experimental details

Amorphous carbon (a–C) thin films were synthesized by direct current (DC) magnetron sputter deposition onto thermally oxidized silicon wafers (oxide thickness larger than 700 nm). Experiments were performed under high vacuum conditions (base pressure of the system $3 \cdot 10^{-6}$ mbar or better). a–C films were deposited using Ar flow rates and sputtering powers of 15 sccm and 100 W, respectively, resulting in ≈92 nm thick films deposited in 1 h. Sputtering was preceded by ≈15 min presputtering performed with identical condition, but without

D. T. Hoffmann, J. Dietrich, S. Mändl, S. G. Mayr
Leibniz-Institut für Oberflächenmodifizierung e.V. (IOM)
Permoserstr. 15,, 04318 Leipzig, Germany
E-mail: stefan.mayr@iom-leipzig.de
D. T. Hoffmann, J. Dietrich, S. G. Mayr
Division of Surface Physics
University of Leipzig
Linnestr. 5, 04103 Leipzig, Germany
M. Zink
Research Group Biotechnology and Biomedicine
Peter-Debye-Institute for Soft Matter Physics
University of Leipzig
Linnestr. 5 04103 Leipzig, Germany

The ORCID identification number(s) for the author(s) of this article can be found under https://doi.org/10.1002/adts.202100093

DOI: 10.1002/adts.202100093

deposition onto the substrate utilizing a shutter in front of the substrate.

Ion implantation was subsequently performed using ultra high vacuum conditions with an IBS IMC 200 linear ion accelerator using 150 keV Ar^+ ions and fluences of $2 \cdot 10^{16}$ and $4 \cdot 10^{16}$ cm^{-2} at temperatures between 150 °C and 350 °C. For temperature calibration, a Peltier element was placed at the sample position and directly exposed to the ion beam, while the beam current was adjusted to obtain the desired sample temperature in steady state condition; the implantation times thus varied between 10 and 179 min. Our choice of ion species, energy and sample thickness was a compromise within our equipments' experimental capabilities to ensure a most homogenous irradiation of the a–C film while implanting the Ar^+ ions into the substrate and minimizing ion beam mixing at the interface, as inferred from SRIM[16] runs (using the standard parameters). While sputtering certainly was present during implantation, it was of minor relevance for the scenario investigated within the current studies (≈27 Å for the maximum fluence $4 \cdot 10^{16}$ cm^{-2}).

Amorphicity of the films was verified prior and after implantation by absence of any indications for crystalline peaks in X-ray diffraction (XRD) measurements using a Rigaku Ultima IV. Morphological evolution was monitored using a Carl Zeiss Ultra 55 scanning electron microscope (SEM) (10 kV acceleration voltage); to check for potential contamination, energy dispersive X-ray analysis is routinely performed, as implemented in this SEM.

3. Experimental Nanoporous Morphogenesis

Ion fluence versus substrate temperature was systematically varied within the ranges given in Section 2 and the impact on morphology explored; a previous preliminary study performed within our group[17] had indicated the absence of pronounced morphological changes at lower doses and temperatures. **Figure 1** illustrates the central results of our fluence–temperature series: Surface morphologies of as deposited a–C films are characterized by very smooth surfaces,[18] which is typical for amorphous films due to the absence of mosaic structure, particularly when sputter deposited.[19,20] Implantation of 150 keV Ar^+ ions does not lead to significant morphological changes at low enough temperatures ($\lessapprox$ 250 °C) and fluences ($\lessapprox 1 \cdot 10^{16}$ cm^{-2}, except for a slight roughness increase that can be attributed to sputter erosion induced kinetic roughening. However, exceeding these thresholds ($T \gtrapprox 300$° C for $\Theta = 2 \cdot 10^{16}$ cm^{-2} and $T \gtrapprox 260$ °C for $\Theta = 5 \cdot 10^{16}$ cm^{-2}) self-organized evolution of a nanoporous morphology is observed. It must be mentioned that $2 \cdot 10^{16}$ cm^{-2} at 300 °C were reached within 10 min with the heating phase encompassing 9 min whereas $4 \cdot 10^{16}$ cm^{-2} at 150 ° C needed 3 h for implantation. To finally wrap up the physical key message, nanoporous morphogenesis requires i) an incubation dose and ii) sufficient thermally induced kinetics.

4. Classical Molecular Dynamics Simulations

We employ our group-maintained highly parallelized classical molecular dynamics (MD) code[21] to prepare amorphous cells of 32768 carbon atoms by rapid quenching melt from 8000 K down to 10 K at rates of 1 K ps^{-1} and zero pressure, utilizing Berendsen thermo- and barostats,[22] respectively, and periodic boundary

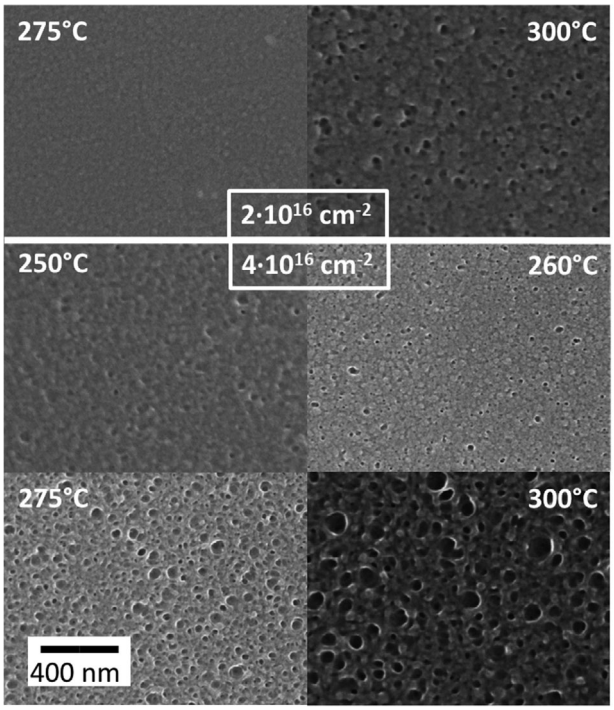

Figure 1. Scanning electron microscopy (SEM) measurements of a–C film implanted with $2 \cdot 10^{16}$ cm^{-2} and $4 \cdot 10^{16}$ cm^{-2} Ar^+ ions, corresponding to damage doses of ≈8.5 dpa and ≈17 dpa, respectively, at different temperatures. Nanoporous morphology starts getting apparent for temperatures $\gtrapprox$ 275 °C and $\gtrapprox$ 260 °C, respectively.

conditions applied in all spatial directions. In doing so, we utilize two alternative empirical bond-order potentials due Brenner (Potential II)[23] and Tersoff[24] with omitted λ_3–correction as in the original publications, yielding glass transitions at $T_g = (2521 \pm 5)$ K and (3817 ± 5) K, respectively. Amorphicity of the resulting cells is subsequently confirmed by evaluating the pair and angular distribution functions, which reveal absence of angular as well as long-range translational order with no significant differences between both potentials.

Regarding implantation of 150 keV Ar^+ ions into amorphous carbon (a–C), as realized within our experiments, we first note that extended thermal spikes are not expected to occur due the relatively low materials density, as reflected also in moderate nuclear and electronic stopping powers, in combination with the relatively high glass transition temperatures, T_g. It is therefore reasonable to assume that implantation induced materials modification under the present conditions is governed by the introduction of point defects. As the latter are strictly defined only in crystalline materials, a major caveat has to be addressed here when dealing with amorphous materials. For a concise definition, we introduce "generalized" vacancies and interstitials (which we solely term "vacancies" and "interstitals" in the following) as atoms with under- and overcoordination, respectively, while a "generalized" Frenkel pair constitutes a combination of both entities. To model the impact of ion implantation under the present conditions, we follow our previous approach (described in detail in ref. [25]) in inserting Frenkel pairs up to the desired defect dose (measured as "displacements per atoms" - dpa) randomly into the simulation

cell. As detailed in ref. [25], interstitials are inserted by replacing an atom by a two-atom dumbbell with a randomly chosen orientation, while vacancies are realized by merely removing an atom.

Interstitials within our generalized definition are manifested by local overcoordination and thus constitute local configurational instabilities due to the presence of dangling bonds that subsequently relax athermally by reconfigurations typically within the nearest and next nearest neighbor shells, resulting in incorporation viz., "absorption" of the interstitial into the surrounding amorphous matrix. While we observe this behaviour presently for both potentials, Brenner II and Tersoff, it is in line also with our previous report on interstitials in amorphous Si-Ge compounds.[13] We choose the variable L_I to denote the average radius around an interstitial affected during the absorption event by the matrix. Vacancies in a–C, on the other hand, are related to presence of multiple bonds among the surrounding atoms due to the strong tendency for hybridization (primarily sp^2 hybridization) in C. While vacancies are thus localized and of reasonable stability, they are expected to be mobile via thermally activated diffusion. Diffusional dynamics of vacancies and their impact on materials modification is clearly beyond the time scale accessible in MD (some μs), but will certainly be highly relevant on experimental time scales. Contrary to single vacancies that perform a random walk in large simulation cells, presence of more than one vacancy will lead to attraction, viz. directed diffusion towards each other due to a corresponding gradient of the chemical potential established by elastic interactions. We characterize this scenario by the the average migration length of a vacancy prior to agglomeration, L_V. To account for sufficient vacancy diffusion in our model despite the restrictions that are inherent to MD in terms of simulated time, we inserted a vacancy directly next to another vacancy, if the latter was located within a distance of L_V within the target site – thus realizing a maximum vacancy relaxation distance as large as L_V (i.e. an inserted vacancy is attached next to an existing one if located within a distance $r \leq L_V$).

For as quenched a–C cells with atomic interactions parameterized due to Brenner II and Tersoff, respectively, we monitor change in cell size upon random insertion of Frenkel pair, while maintaining temperatures at 10 K and zero pressures, respectively. As visualized in **Figure 2**, the average volumes per atom, $< \Omega >$ show a continuous increase as function of dose only for vacancy relaxation lengths, $L_V \gtrapprox 5$ Å, while a constant level (saturation) of $< \Omega >$ after a small initial increase is observed as a function of dose for $L_V \lessapprox 2.5$ Å. Representative configurational snapshots of the morphological evolution are shown in **Figure 3**. As central point it deserves emphasizing here that nanoporous morphogenesis in a–C requires vacancy relaxation distances L_V beyond a threshold level of ≈5 Å or, equivalently, temperature to exceed a certain threshold temperature to allow for the necessary diffusion—which completely complies with the experimental observations. For lower L_V or, equivalently, lower temperatures than the threshold, a steady state is reached in which Frenkel pair insertion and annihilation are balanced. The (dynamically constant) defect concentration inherent to the latter phase generates the moderate volume increase at low doses and moderately elevated volume levels in comparison to the as quenched solid (Figure 2). In terms of L_V and L_I, the "critical point" for nanoporous morphogenesis is thus given by $L_V \approx L_I$, that is, nanoporous pattern formation occurs, if the length scale for vacancy diffusion

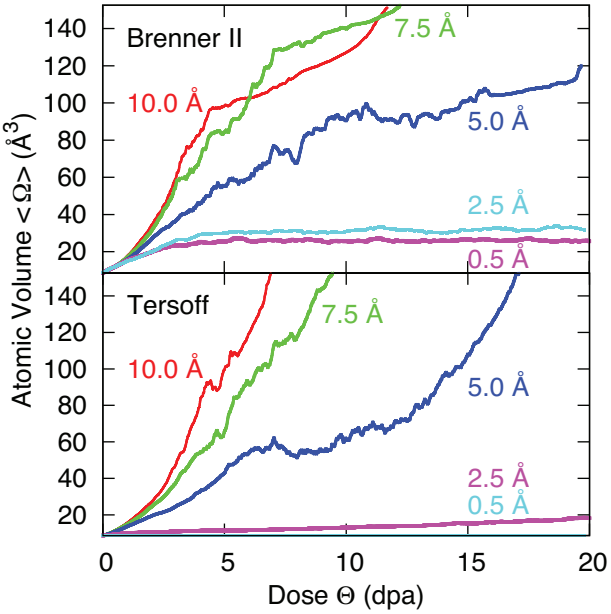

Figure 2. Changes of average volumes per atom, $< \Omega >$, due to random insertion of Frenkel pairs, as a function of the vacancy relaxation distance, L_V, calculated for the Brenner II and Tersoff potentials. Nanoporous morphogenesis is only observed for $L_V \gtrapprox 5.0$ Å.

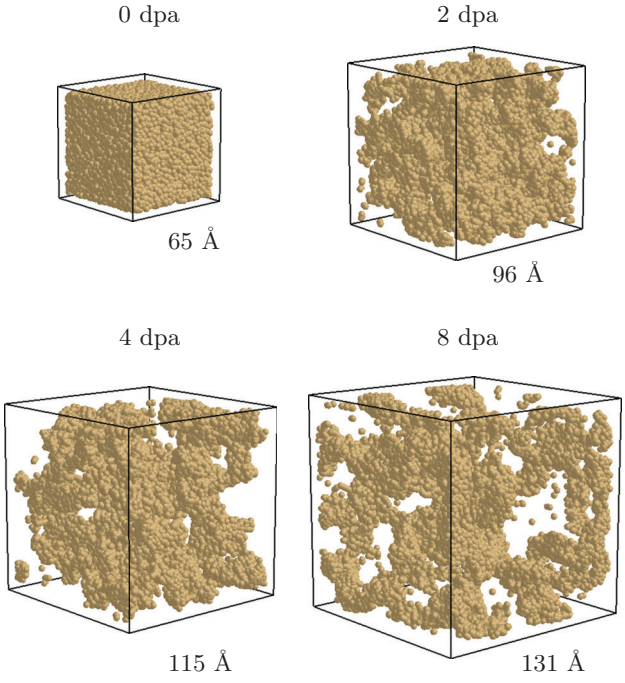

Figure 3. 3D configurational snapshots during Frenkel pair induced nanoporous morphology evolution: ($L_V = 5$ Å).

exceeds the dimensions of the regions involved in absorption of an interstitial. As the process of interstitial absorption can be biased by applied shear stresses, it constitutes a local shear event capable to locally relax shear stresses, while vacancies themselves reveal much less local reconfigurations to reduce shear stress.

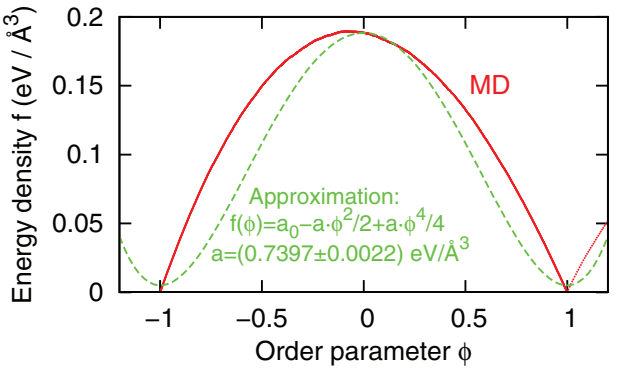

Figure 4. Approximate fit of the free energy density f as a function of order parameter ϕ (Equation (1)) to MD predictions using the Brenner II potential, as obtained by inserting vacancies and interstitials, respectively, into a–C cells, keeping the volume fixed.

It is worth mentioning here, that—concerning viscous flow—we have observed as similar behavior of vacancies and interstitials in amorphous Ge (ref. [26], Figure 9 – interstitials are much more effective in stress relaxation than vacancies in dense amorphous Ge). Vice versa, the process of vacancy-interstitial annihilation by interstitial-induced matrix reconfiguration can be cast into the picture of pore closure by radiation induced viscous flow, as discussed in detail for the Si–Ge system in ref. [13].

5. Cahn–Hilliard Model

Previously Cahn–Hilliard type of models have successfully been employed to model radiation induced effects in matter, including pattern formation in driven alloys[27,28] and crystalline void lattices.[29] Our MD model (Section 4) together with our previous studies[13,25] clearly suggests that nanoporous morphogenesis is goverend by i) introduction of Frenkel pairs into the amorphous matrix, ii) athermal relaxation and "absorption" of interstitials by the amorphous matrix while mediating radiation induced viscous flow, iii) thermally activated migration and agglomeration of vacancies initially dispersed randomly within the matrix. As in particular iii) is reminiscent of a spinodal decomposition process, it becomes tempting to apply a Cahn–Hilliard[30] type of model on the amorphous "alloy" "composed" of C and vacancies to model nanopore morphogenesis in a–C upon ion implantation. A central ingredient within this scope is the possibility to define a free energy density, f as function of a suitable order parameter, ϕ. While we define the latter as $\phi = 2 \cdot \nu_V - 1$, where ν_V denotes the vacancy atomic concentration, we choose as functional form for the free energy density functional,

$$f(\phi) = -\frac{a}{2}\,\phi^2 + \frac{a}{4}\,\phi^4 \tag{1}$$

where a denotes a fitting parameter. Assuming that it is reasonable for us to neglect the entropy contributions due to the rather moderate temperatures employed in experiments and simulations, we fit Equation (1) to the internal energy determined via MD as a function of vacancy concentration at fixed volume, as shown in **Figure 4**.

While the functional form for $f(\phi)$ is clearly too simple to "exactly" account for the MD predictions, it is nevertheless capable of reproducing key characteristics; in the first place the maximum at $\phi = 0$ and minima at $\phi = \pm 1$ that correspond to "equilibrium" vacancy concentrations of $\nu_V = 0$ and $\nu_V = 1$, viz. a defect–free amorphous solid and vacuum as equilibrium phases. In the presence of spatially varying order parameter, $\phi(\vec{r})$, an interface energy contribution $\frac{1}{2}(W_0\,\nabla\phi)^2$ needs to be considered in addition to the terms of Equation (1); in equilibrium $\phi(\vec{r})$ is then given by minimizing the free energy functional

$$F[\phi(\vec{r})] = \int d^3r \left(f\left(\phi(\vec{r})\right) + \frac{1}{2}\,W_0^2\,(\nabla\,\phi)^2 \right) \tag{2}$$

that is, by equalizing the functional derivative to zero. In the presence of a flat equilibrium interface between equilibrium vacuum and solid, respectively, the equilibrium order parameter can readily be determined for the interface region,[31] enabling us to relate a (Equation (1)) and W_0 (Equation (2)) to the surface energy

$$\sigma = W_0\,\frac{2\sqrt{2}}{3}\,\sqrt{a} \tag{3}$$

yielding $W_0 = 0.2148\,\sqrt{\frac{\mathrm{eV}}{\mathrm{Å}}}$.

Up to this point, we have developed a formalism and fitted parameters to describe the free energy of the vacancy – a–C system as functional of an arbitrary vacancy distribution, described by order parameter, $\phi(\vec{r})$, while central ingredients—in particular interstitials and dynamics—are still missing. Within a next step, we now focus on vacancy dynamics, omitting still the presence of interstitials. Except for the irradiation source term, the number of atoms and vacancies within the cell is conserved; we therefore employ Model B dynamics[32] for spatio–temporal evolution, supplemented by an average flux (I) and noise ($\eta(\vec{r},t)$) term, viz

$$\frac{\partial\,\phi}{\partial t} = \underbrace{\Pi\,\nabla^2\left(-W_0^2\,\nabla^2\,\phi + a\,\phi\left(\phi^2-1\right)\right)}_{=\Pi\,\nabla^2\,\frac{\delta F[\phi]}{\delta\phi}} + I + \eta\left(\vec{r},t\right) \tag{4}$$

where δ indicates variational derivatives and the Euler–Lagrange equations in combination with Equations (1) and (2) have been used. The generalized mobility, $\Pi = 4\,\Omega_0\,\mu$, is related to the atomic volume within the dense phase, Ω_0 and mobility, μ (the prefactor 4 appears here due to the definition of the order parameter). To estimate μ, we consider a vacancy close to an open surface (such as the surface of a pore), that is, assumed to be flat for simplicity. Due to Bacon (ref. [33], Equation (26)) the energy of a vacancy that resides a distance, d, away from the surface is then given by

$$E(d) = -\frac{(1-2\,\nu)^2\,P^2}{16\,\pi\,(1-\nu)\,G\,d^3} \tag{5}$$

where G, ν, and P denote the shear modulus, Poisson's ratio and dipole moment, respectively. If we assume that the vacancy is initially a distance, $d = L_V$ (compare Section 4) apart from the surface, subsequently migrates toward it and reaches and joins it (we somewhat arbitrarily choose $d = 2\,r_A$ for this event, where

Table 1. Summary of materials constants that were determined for a–C using the Brenner II potential for estimation of the generalized mobility, Π.

G (eV/Å^3)	ν	P (eV)	L_V (Å)	r_A (Å)	Π (Å^5/eV)
0.432	0.368	2.07	5	1.269	$2.522 \cdot 10^7$

$\Omega_0 = 4/3 \cdot \pi\, r_A^3$), the average force on the vacancy throughout this process is given by $\langle K \rangle = (E(L_V) - E(2\,r_A))/(L_V - 2\,r_A)$. Following the suggestions of our MD model (Section 4), vacancy diffusion terminates, once within a radius of L_I of an inserted interstitial. Assuming that the sample temperature is chosen close to the critical temperature, $L_I \approx L_V$ (see Section 4), yielding an average diffusion time (measured in "time" units of dose) of $\Theta_D = \Omega_0/(4/3\,\pi\, L_V^3)$. Thus, the average vacancy velocity can be calculated as $\langle v \rangle = (L_V - 2\,r_A)/\Theta_D$. Merging things together, we finally obtain for the generalized mobility

$$\Pi = \frac{16\,\pi\left(L_V - 2\,r_A\right)^2 L_V^3}{3\left(E\left(L_V\right) - E\left(2\,r_A\right)\right)} \tag{6}$$

We determined all materials constants appearing in Equations (5) and (6) for the Brenner II potential using MD, while we chose L_V consistent with the "critical" value determined in Section 4; the full parametrization is summarized in **Table 1**. Maybe determination of the dipole moment deserves mentioning an extra remark—it was based on determination of stress change, $\Delta\sigma_{ij}$, in a cell with fixed geometry upon defect insertion, utilizing the relation $\Delta\sigma_{ij} = (c/\Omega_0)P_{ij}$ (see, e.g., ref. [34], Equation (8); c denotes the atomic density of statistically distributed point defects), which proved to be isotropic.

While the average flux term for vacancy insertion ($I = -2$) in Equation (4) is straightforward, when measuring time in units of dose, the noise term, $\eta(\vec{r}, t)$ accounts for accompanying spatiotemporal fluctuations and will be discussed in more detail in the following. Generally, $\eta(\vec{r}, t)$ is understood as spatially and temporally uncorrelated (i.e., white) Gaussian noise of average zero, that is

$$\left\langle \eta\left(\vec{r}, t\right) \right\rangle = 0 \tag{7}$$

$$\left\langle \eta\left(\vec{r}, t\right) \eta\left(\vec{r}', t'\right) \right\rangle = 2\,D\,\delta\left(\vec{r} - \vec{r}'\right)\delta\left(t - t'\right)$$

Generally, the problem of randomly removing atoms can be regarded as Bernoulli experiment, that follows the binominal distribution with variance $2\,I$; D is determined to yield the same second moment, resulting in $D = 2\,\Omega_0$, when employing dose as measure for time (mind that the definition of the phase field also enters the magnitude of D). Regarding noise and its implementation during numerical solution of our Cahn–Hilliard equation, one further point deserves mentioning here: while $\langle \eta(\vec{r}, t) \rangle$ is originally defined as Gaussian white noise, numerical tests of several groups (e.g., ref. [35] and in the scope of ref. [19]) have revealed that statistically identical results are obtained, when equally distributed random numbers of the same first and second moments are employed instead. We will make use of this finding when numerically solving our present model.

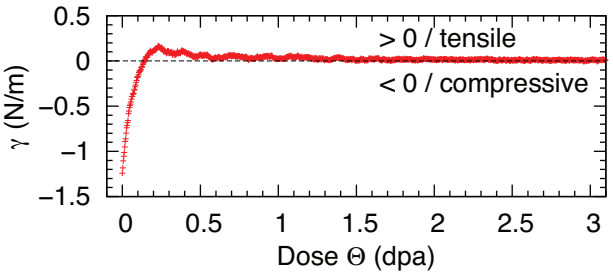

Figure 5. Evolution of surface stress, γ, with increasing dose, Θ, as described by the Brenner II potentials.

Up to this point, the contribution of interstitials to nanoporous morphogenesis has not been taken into account within the Cahn–Hilliard model. Our MD calculations (Section 4) suggest that interstitials affect morphological evolution in a threefold way: i) interstitials, that are introduced into a–C, annihiliate with vacancies and thus lead to a conversion of the effective to real doses by applying a factor of $\approx 1/(1 + (I/2) \cdot t)$ (based on the simplistic assumption that the probability of annihilation of an introduced interstitial is proportional to the vacancy concentration in the system). ii) If not annihilated by interaction with vacancies, interstitials are "absorbed" by the matrix, leading (on average) to an isotropic volume increase (in the sense of an "upscaling") of the cell and all its features in all spatial directions by one atomic volume, Ω_0; the number of interstitials contributing to this effect equals the number of vacancies remaining in the matrix. iii) The processes of annihiliation (i) and matrix "absorbance" (ii) becomes biased in presence of shear stresses primarily due to capillarity, that is, the evolved volume constitutes a type of shear transformation zone[21] that performs a local flow event and results in structure relaxation driven by surface stress, γ (mind within this context, that surface stress and energy have to be distinguished in solids). As shown in **Figure 5**, γ is clearly affected by dose due to structural remodelling of surface, yielding a steady state, $\gamma = 0$ for sufficiently large doses, indicating large absence of capillarity. Based on this finding, we will neglect (iii) in the following.

We base our phase field treatment of ion implantation induced morphogeneis in a–C on Equations (4) and (7) using the parametrization of Table 1. As this model only describes vacancy dynamics, it needs to be supplemented by the effects (i) and (ii) related to interstitials, as discussed above. While i) vacancy–interstitial annihilation is considered by measuring only insertion of stable defects, that is, effective defect doses, ii) incorporation of interstitials into the matrix is realized by enlarging the cell volume isotropically by Ω_0 per inserted interstitial, yielding an increase of cell volume by a factor of $1/(1 + (I/2)\,t)$. Starting with cubic cells of initial edge lengths, L_0 with periodic boundaries applied in all spatial directions, absorption of interstitials by the matrix thus leads to edge lengths $L = L_0/(1 + (I/2)\,t)^{1/3}$ increasing as a function of dose—just as all linear dimension do within the cell. Defects clearly can only be inserted into a–C material (not into vacancies or vacancy agglomerates); furthermore, as the total amount of a–C remains conserved within the cell during volume change, so does the number of Frenkel pairs introduced into the cell per time increment. We take this into account by weighting I and η in Equation (4) by $(\mathrm{sgn}(\Phi) + 1)/2$, where sgn denotes the

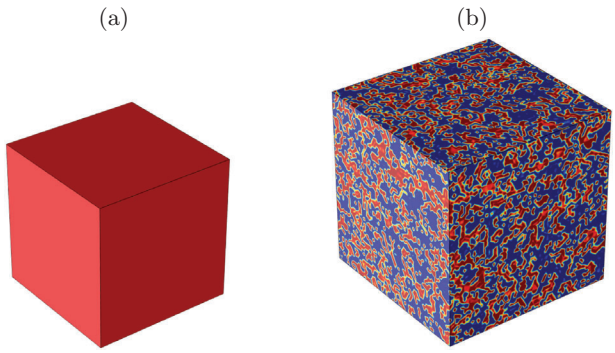

Figure 6. Solutions of the phase field model (Equation (8)) after exposure to doses of a) 0 dpa, b) 8.0 dpa. Color codings range from blue ($\phi = -1$) to red ($\phi = +1$), the edge lengths of the cubic boxes increase from a) 500.0 nm to b) 619.3 nm, respectively.

sign function. The total equation we solve in the following thus reads

$$\frac{\partial \phi}{\partial t} = \Pi \cdot \left(1 + \frac{I}{2} t\right)^{2/3} \tag{8}$$

$$\nabla^2 \left(-W_0^2 \cdot \left(1 + \frac{I}{2} t\right)^{2/3} \cdot \nabla^2 \phi + a\, \phi \left(\phi^2 - 1\right) \right) + \frac{\mathrm{sgn}(\phi) + 1}{2} \cdot \left(I + \eta(\vec{r}, t)\right)$$

Free tetrahedral meshes with $\approx 4 \cdot 10^5$ elements, as implemented in COMSOL,[36] are employed for spatial discretization using a element discretization order of 2, while—due to the stochastic nature of the equation—the simple Euler method is employed for numerical integration utilizing a time step of $5 \cdot 10^{-4}$ dpa, as confirmed by spatiotemporal convergence tests.[37]

Figure 6 illustrates the results of the numerical solution of our phase field model that reveals pronounced formation of a nanoporous structure, starting from small "nuclei" followed by successive coarsing. Clearly spatiotemporal dynamics reveals some similarities to deterministic Model B dynamics[32] and even more to their noisy generalizations (see, e.g., ref. [31])—in the sense that a linear instability with maximum pattern growth at $\lambda_{max} = 2\pi\sqrt{-(2\, W_0^2)/f''(\phi_0)}$ underlies also the presently observed pattern formation. However, due to the dynamic character of defect insertion and box volume change, things are clearly more complex presently.

Regarding comparison with our MD model (Section 4), nanoporous pattern formation clearly occurs on similar length scales in the early stages of morphogenesis, but starts to deviate once the typical pore size reaches the dimension of the MD cell. These finite size effects thus can clearly be overcome in our coarse-grained phase field model, that is indeed suitable to establish a link to experimental results, that is, the "real" world.

Regarding experiments, our results (Figure 6) need to be compared with samples where pattern formation is just starting to occur, as we have chosen L_V accordingly. In this sense, our modelling is in accordance with, for example, Figure 1, which reveals porous patterns on length scales in the same order of magnitude. Higher temperatures in the experiments will clearly lead to increasing L_V, and thus accordingly lead to an increase of length scale of our nanostructured morphology as well.

6. Conclusion

To conclude, we have demonstrated within our present work that ion implantation into sputter deposited thin a–C films can successfully be employed to generate tailored nanoporous morphologies. Using a combined experimental and scale-bridging computational approach, which employs MD and a phase field type of model, we unravel the physics underlying nanoporous morphogenesis. Experimentally a minimum temperature of $\gtrapprox$ 260 °C and incubation dose as large as ≈8 dpa are required; below these thresholds no nanoporous structure formation can be observed. Within the framework of our models, nanoporous pattern formation results from self-organization of Frenkel pairs, that are introduced into a–C in course of implantation. If Frenkel pairs do not annihilate athermally directly after insertion, interstitials are athermally absorbed by the a–C matrix; while this absorption process leads on average to an "upscaling" of the cell volume by Ω_0, it becomes biased in the presence of applied stresses, leading to radiation induced flow. Vacancies on the other hand constitute stable entities, that show a spinodal-like decomposition behavior if a sufficiently high temperature for significant vacancy diffusion is reached. In particular, the typical vacancy diffusion length needs to exceed the length scale below which spontaneous vacancy-interstitial annihilation occurs—which determines the temperature threshold for nanoporous morphogenesis. Our developed picture also provides a concise explanation for the experimentally observed incubation dose, viz. it constitutes a homogeneous nucleation scenario, in which a barrier due to surface energy needs to be overcome successfully, as treated in many textbook classical binary alloys.

As we have demonstrated and explained the physics underlying implantation induced nanoporous morphogenesis in a–C, our findings pave the way for tailored synthesis of nanoporous thin films and nanostructures. As the employed technologies, sputtering and implantation, are established in semiconductor industry, we envision potential also for on–chip integration.

Acknowledgements

The authors would like to thank Dr. F. Lehnert and T. Isensee for further studies within the field, which, however, did not enter the present manuscript, as well as Dr. J. Gerlach and Dr. J. Bauer for help with X-ray and SEM measurements. Funding in parts by the Deutsche Forschungsgemeinschaft (DFG – project MA 2432/5-1) and German Ministry of Science and Education (BMBF), project EYECULTURE, FKZ 031A574C is gratefully acknowledged.

Open access funding enabled and organized by Projekt DEAL.

Conflict of Interest

The authors declare no conflict of interest.

Data Availability Statement

Data available on request from the authors.

Keywords

ion implantation, molecular dynamics, nanoporous carbon, phase field model, self-organized structure formation, sponge

Received: March 19, 2021
Revised: April 26, 2021
Published online: June 2, 2021

[1] Y. Zhu, S. Murali, M. D. Stoller, K. Ganesh, W. Cai, P. J. Ferreira, A. Pirkle, R. M. Wallace, K. A. Cychosz, M. Thommes, D. Su, E. A. Stach, R. S. Ruoff, *Science* **2011**, *332*, 1537.
[2] K. Jayaramulu, D. P. Dubal, B. Nagar, V. Ranc, O. Tomanec, M. Petr, K. K. R. Datta, R. Zboril, P. Gómez-Romero, R. A. Fischer, *Adv. Mater.* **2018**, *30*, 1705789.
[3] S. Ott, A. Orfanidi, H. Schmies, B. Anke, H. N. Nong, J. Hübner, U. Gernert, M. Gliech, M. Lerch, P. Strasser, *Nat. Mater* **2020**, *19*, 77.
[4] Y. Yang, K. Chiang, N. Burke, *Catal. Today* **2011**, *178*, 197.
[5] S. J. Yang, T. Kim, J. H. Im, Y. S. Kim, K. Lee, H. Jung, C. R. Park, *Chem. Mater.* **2012**, *24*, 464.
[6] A. Stein, Z. Wang, M. A. Fierke, *Adv. Mater.* **2009**, *21*, 265.
[7] J. Lee, J. Kim, T. Hyeon, *Adv. Mater.* **2006**, *18*, 2073.
[8] I. H. Wilson, *J. Appl. Phys.* **1982**, *53*, 1698.
[9] B. Stritzker, R. Elliman, J. Zou, *Nucl. Instrum. Methods Phys. Res. B* **2001**, *175–177*, 193.
[10] R. Böttger, K.-H. Heinig, L. Bischoff, B. Liedke, S. Facsko, *Appl. Phys. A* **2013**, *113*, 53.
[11] M. C. Ridgway, T. Bierschenk, R. Giulian, B. Afra, M. D. Rodriguez, L. L. Araujo, A. P. Byrne, N. Kirby, O. H. Pakarinen, F. Djurabekova, K. Nordlund, M. Schleberger, O. Osmani, N. Medvedev, B. Rethfeld, P. Kluth, *Phys. Rev. Lett.* **2013**, *110*, 245502.
[12] K. Gärtner, J. Jöhrens, T. Steinbach, C. S. Schnohr, M. C. Ridgway, W. Wesch, *Phys. Rev. B* **2011**, *83*, 224106.
[13] F. Lehnert, S. G. Mayr, *Phys. Chem. Chem. Phys.* **2017**, *19*, 23461.
[14] C. Cawthorne, E. Fulton, *Nature* **1967**, *216*, 575.
[15] J. Evans, *Nature* **1971**, *229*, 403.
[16] J. Ziegler, J. Biersack, M. Ziegler, *SRIM, the Stopping and Range of Ions in Matter*, SRIM Company, **2008**.
[17] F. Lehnert, *Strukturänderung kovalenter Materialien durch Ionenbestrahlung*, Dissertation, Universität Leipzig, Germany **2018**.
[18] SEM topographies of as deposited films are indistinguishable from those measured for $2 \cdot 10^{16}$ cm^{-2} and 275 K as shown in the topmost picture on the r.h.s. in Figure 1.
[19] S. G. Mayr, M. Moske, K. Samwer, *Phys. Rev. B* **1999**, *60*, 16950.
[20] S. G. Mayr, K. Samwer, *J. Appl. Phys.* **2002**, *91*, 2779.
[21] S. G. Mayr, *Phys. Rev. Lett.* **2006**, *97*, 195501.
[22] H. J. C. Berendsen, J. P. M. Postma, W. F. van Gunsteren, A. DiNola, J. R. Haak, *J. Phys. Chem.* **1984**, *81*, 3684.
[23] D. W. Brenner, *Phys. Rev. B* **1990**, *42*, 9458.
[24] J. Tersoff, *Phys. Rev. Lett.* **1988**, *61*, 2879.
[25] S. G. Mayr, Y. Ashkenazy, K. Albe, R. S. Averback, *Phys. Rev. Lett.* **2003**, *90*, 055505.
[26] S. G. Mayr, R. S. Averback, *Phys. Rev. B* **2005**, *71*, 134102.
[27] G. Martin, *Phys. Rev. B* **1984**, *30*, 1424.
[28] G. Martin, P. Bellon, Driven alloys, in *Advances in Research and Applications* (Eds: H. Ehrenreich, F. Spaepen), Solid State Physics, Vol. *50*, Academic Press, **1996**, pp. 189–331.
[29] Y. Gao, Y. Zhang, D. Schwen, C. Jiang, C. Sun, J. Gan, *Materialia* **2018**, *1*, 78.
[30] J. W. Cahn, J. E. Hilliard, *J. Chem. Phys.* **1958**, *28*, 258.
[31] N. Provatas, K. Elder, *Phase-field methods in materials science and engineering*, John Wiley & Sons, **2011**.
[32] P. C. Hohenberg, B. I. Halperin, *Rev. Mod. Phys.* **1977**, *49*, 435.
[33] D. J. Bacon, *Phys. Stat. Sol. (b)* **1972**, *50*, 607.
[34] P. Dederichs, C. Lehmann, H. Schober, A. Scholz, R. Zeller, *Journal of Nuclear Materials* **1978**, *69–70*, 176.
[35] K. Moser, J. Kertész, D. E. Wolf, *Physica A* **1991**, *178*, 215.
[36] Comsol, Comsol Inc. (www.comsol.com).
[37] It deserves mentioning here that the step function in Equation (8) was realized using flc2hs, as implemented in COMSOL.